Marine Pollution Bulletin 173 (2021) 112996

Contents lists available at ScienceDirect

Marine Pollution Bulletin

journal homepage: www.elsevier.com/locate/marpolbul

Investigation into the geometry and distribution of oil inclusions in sea ice using non-destructive X-ray microtomography and its implications for remote sensing and mitigation potential

Durell S. Desmond [a,*], Odile Crabeck [b,c,d], Marcos Lemes [a], Madison L. Harasyn [a], Amirbahador Mansoori [a], Diana Saltymakova [a], M. Christopher Fuller [a,e], Søren Rysgaard [a,f], David G. Barber [a], Dustin Isleifson [a], Gary A. Stern [a,*]

[a] University of Manitoba, Winnipeg, MB, Canada
[b] University of East Anglia, Norwich, United Kingdom
[c] Laboratoire de Glaciologie, Université Libre de Bruxelles, Bruxelles, Belgium
[d] Unité d'Océanographie Chimique, Freshwater and Oceanic sCience Unit reSearch (FOCUS), Université de Liège, Liège, Belgium
[e] University of Calgary, Calgary, AB, Canada
[f] Aarhus University, Aarhus, Denmark

ARTICLE INFO

Keywords:
Sea ice
Oil-in-ice
Crude oil
X-ray imaging
Remote sensing detection
Bioremediation

ABSTRACT

As climate change brings reduced sea ice cover and longer ice-free summers to the Arctic, northern Canada is experiencing an increase in shipping and industrial activity in this sensitive region. Disappearing sea ice, therefore, makes the Arctic region susceptible to accidental releases of different types of oil and fuel pollution resulting in a pressing need for the development of appropriate scientific knowledge necessary to inform regulatory policy formulation.

In this study, we examine the microstructure of the surficial layers of sea ice exposed to oil using X-ray microtomography. Through analysis, 3D imaging of the spatial distribution of the ice's components (brine, air, and oil) were made. Additional quantitative information regarding the size, proximity, orientation, and geometry of oil inclusions were computed to ascertain discernable relationships between oil and the other components of the ice. Our results indicate implications for airborne remote sensing and bioremediation of the upper sea ice layers.

1. Introduction

Within the Arctic, anthropogenic global warming has led to continual decreases in sea-ice extent, thickness, and changes in ice type (IPCC, 2014; AMAP, 2017). Shipping and oil exploration are, therefore, becoming increasingly more feasible, thereby increasing the potential of crude oil or fuel being spilled into the marine environment (AMAP, 2010; Schenk, 2011; Smith and Stephenson, 2013; Harsem et al., 2011). This impending possibility has generated a need for the development of oil detection and mitigation techniques suitable for ice-covered waters (Fritt-Rasmussen et al., 2015; Brown and Fingas, 2003; Brekke et al., 2014; Wilkinson et al., 2015; Bradford et al., 2015; Firoozy et al., 2017; Hubert and Stern, GENICE).

Sea ice is a heterogeneous porous media consisting of an ice matrix that is embedded with liquid brine inclusions, solid salts, and air bubbles. The presence of brine networks and air inclusions strongly influence the electromagnetic properties of the ice, thus impacting incident electromagnetic responses used in remote sensing detection and characterization (Fingas and Brown, 2007). Notably, the brine inclusions are often sites of biological activity (Fritsen et al., 1994; Krembs et al., 2000; Vancoppenolle et al., 2013). The abundance, distribution, and structure of brine and air inclusions are strongly dependent on the temperature and salinity of the sea ice. Its thermodynamic history, as well as its surface features (e.g., snowfall, frost flowers, and surface roughness) also play a major role (Cox and Weeks, 1983; Weeks and Ackley, 1986; Galley et al., 2015). As sea ice has the potential for oil entrainment (Petrich et al., 2013; Maus et al., 2015; Oggier et al., 2019), the inclusion of oil inside the ice matrix will influence the temperature and salinity of

* Corresponding authors.
E-mail addresses: umdesmod@myumanitoba.ca (D.S. Desmond), gary.stern@umanitoba.ca (G.A. Stern).

https://doi.org/10.1016/j.marpolbul.2021.112996
Received 29 June 2020; Received in revised form 21 August 2021; Accepted 19 September 2021
Available online 6 October 2021

the ice and therefore the presence and morphology of the brine and air inclusions (e.g., Payne et al., 1991a; O'Sadnick et al., 2017).

Remote sensing of oil in and on sea ice based on dielectric difference is well established in the literature (e.g., Puestow et al., 2013; Brekke et al., 2014; Firoozy et al., 2017; Firoozy et al., 2018). From past work, it was concluded that it is possible to detect the bulk oil content embedded within the surface of sea ice, using active radar, through the reduction of sea ice salinity caused by brine displacement from upward oil migration through brine channels (Desmond et al., 2019a; Saltymakova et al., 2020). This reduction of salinity lowers the dielectrics and thus the radar signature of sea ice, allowing for a detectable change. Furthermore, physical simulations have been linked to remote sensing of oil-contaminated sea ice previously (e.g., Neusitzer et al., 2018a; Desmond et al., 2019a; Isleifson et al., 2020; Firoozy et al., 2018). In particular, modelling the Normalized Radar Cross-Section (NRCS) of sea ice has been a common practice. The physics of the energy interactions based on real or simulated dielectric differences of oil, brine, and sea ice apply similarly to microwave remote sensing and x-ray tomography.

A moderate amount of research on oil behaviour in sea ice has been conducted over the last few decades (e.g., Fingas and Hollebone, 2003; Brandvik and Faksness, 2009; Ballestero and Magdol, 2011; Faksness et al., 2011; Faksness and Brandvik, 2008; Fritt-Rasmussen et al., 2015; Maus et al., 2015; Petrich et al., 2013; Afenyo et al., 2016a; Afenyo et al., 2016b; Payne et al., 1991a; Payne et al., 1991b; Oggier et al., 2019). Much of this research has focused on bulk physical movement tendencies (macroscopic behaviour) and less on microscopic behaviour within the ice. In order to properly establish detection technologies and mitigation potential (Firoozy et al., 2017; Neusitzer et al., 2018a; Firoozy et al., 2018; Hubert and Stern, GENICE), a better understanding of the movements and interactions of oil in a sea ice environment on a microscopic scale is required. To this end, we present a methodology employing enhanced computed microtomography X-ray imaging for analyzing the microstructure of oil-contaminated sea ice.

Micro-Computed Tomography (μ-CT) X-ray imaging is a non-destructive radiographic technique which examines materials by creating images of density contrast. As dense materials and higher atomic numbers result in greater X-ray attenuation, an image of the target of interest can be created (Duliu, 1999). The resultant image is represented in grayscale whereby darker tones indicate a material of lower density (e.g. air) and lighter tones indicate higher density materials or phases (e.g., brine). Since μ-CT is capable of high-resolution three-dimensional characterization of the internal features of porous media, it has been advantageous for examining the brine and air components of sea ice microstructure (e.g., Crabeck et al., 2016; Golden et al., 2007; Lieb-Lappen et al., 2017; Maus et al., 2013; Maus et al., 2015; Obbard et al., 2009; Pringle et al., 2009; Frantz et al., 2019). Little X-ray work, however, has been conducted on oil-contaminated sea ice (Courville et al., 2017; Bazilchuk, 2018; Salomon et al., 2017). Oil and ice have similar densities producing little contrast in the resultant μ-CT-image (Salomon et al., 2017). Furthermore, small volume fractions of oil relative to the ice can also hinder the distinction between the two phases. Herein we introduce a novel method for the enhanced imaging of oil in sea ice in which we evaluate its qualitative and quantitative capabilities for assessing the oil inclusions and its implications for both remote sensing and bioremediation of oil-contaminated sea ice.

This study builds on the past X-ray work noted above. In particular, Salomon et al. (2017) performed a general analysis on the distribution of oil in the porous space of columnar sea ice. These authors noted that the absorption contrast between oil and ice was insufficient for automatic segmentation. Segmentation was therefore performed manually by tracing each visible oil inclusion within each 2D-slice. This method of analyzing oil inclusions was deemed to be exceedingly time consuming and unrealistic for the investigation of numerous samples. Other works such as (Courville et al., 2017; Maus et al., 2013) have incorporated the use of μ-CT for the purpose of investigating the microstructure of sea ice (e.g., skeletal layer at the water-ice interface) to better understand oil migration through brine channels (i.e., oil infiltration, porosity and permeability). These works were used to improve the modelling of 1) oil entrainment in sea ice (Maus et al., 2015), 2) fluid flow in porous media (Oggier et al., 2019), and 3) waterborne sensor performance (e.g., sonar) in different oil in ice scenarios (Courville et al., 2017). Overall, these works have focused on the bulk migration of oil through columnar sea ice and the remote sensing detection from under and within ice.

In our study, we developed a methodology for the improved detection of oil by μ-CT, facilitating a faster image processing through automatic segmentation. Our focus lies on the frazil/inter-frazil ice layer of sea ice (upper regions) with an emphasis on oil distribution and proximity to air and brine, as well as the geometry of all inclusions. The implications of these results are discussed in the context of 1) airborne remote detection (e.g., radar) of oil-contaminated sea ice, which is influenced by the shape, volume, distribution, and orientation of sea inclusions (Ulaby and Long, 2014); and 2) bioremediation of oil-in-ice which is dependent on the proximity of oil and brine (Vergeynst et al., 2018). In the Northern Arctic, an oil spill is more likely to occur during fall freeze-up with a heightened shipping or industrial activity than mid-winter (Martin, 1979; Oggier et al., 2019; BBC News, 2020). Therefore, the presence of oil in the top part of the sea ice profile is a likely scenario. The findings reported in this paper will be useful for 1) the development of remote sensing algorithms required to detect oil within the surficial sea ice and 2) the development of scientific knowledge required for the planning and coordination of proper mitigation response efforts (e.g., bioremediation) suitable for ice covered waters.

2. Materials and methods

2.1. Source of X-ray samples

Three annual artificial oil-in-ice mesocosm experiments were conducted at the University of Manitoba (UofM) Sea-ice Environmental Research Facility (SERF) during 2016-2018. From these experiments, crude oil-contaminated ice cores were sampled as described in the following works: Desmond et al. (2019b, 2021), Saltymakova et al. (2019, 2020), and Neusitzer et al. (2018b).

Each of the three oil-in-ice mesocosm experiments, from which our samples are derived, exhibited conditions that closely resemble natural sea ice thermodynamic states indicative of Arctic marine waters; that is, the temperature increased towards the water column and the bulk salinity demonstrated a normal C-shape profile. Furthermore, most of the oil that was injected below the ice was found to have migrated towards the ice surface due to the warm ice temperatures (i.e., ≥ -5 °C) (Eicken, 2003; Petrich and Eicken, 2010) and lower density of the oil (860 kg/m^3) relative to that of seawater/brine (>1020 kg/m^3).

Due to variation in atmospheric temperature and snow precipitation during the different experiments (2016, 2017, 2018), the extent of sea ice growth varied for each experiment. The maximum ice thickness over the course of the three experiments was ~60 cm. A general ice stratigraphy analysis was conducted using cores extracted from the ice. Cores were examined visually and photographed to qualitatively determine ice layering and type (i.e., granular or columnar) and were later sliced into horizontal thick sections and vertical thick/thin sections. Crossed optical polarizers were used to analyze the ice microstructure of a relatively clean sample (no visible oil) taken from the SERF 2018 experiment (Desmond et al., 2021). Example photographs depicting the alternations of granular and columnar ice can be seen in Figs. 1 and S1. The influence of oil on sea ice and the potential for the growth of additional granular layers has previously been reported by (Martin, 1979). Most of the X-ray samples investigated herein were taken from locations which were saturated with oil and visually resembled granular or inter-granular ice. A further assessment of the ice type (granular/inter-granular or columnar) corresponding to the X-ray samples is discussed in Section 3.2.1 based on μ-CT computed inclusion orientations.

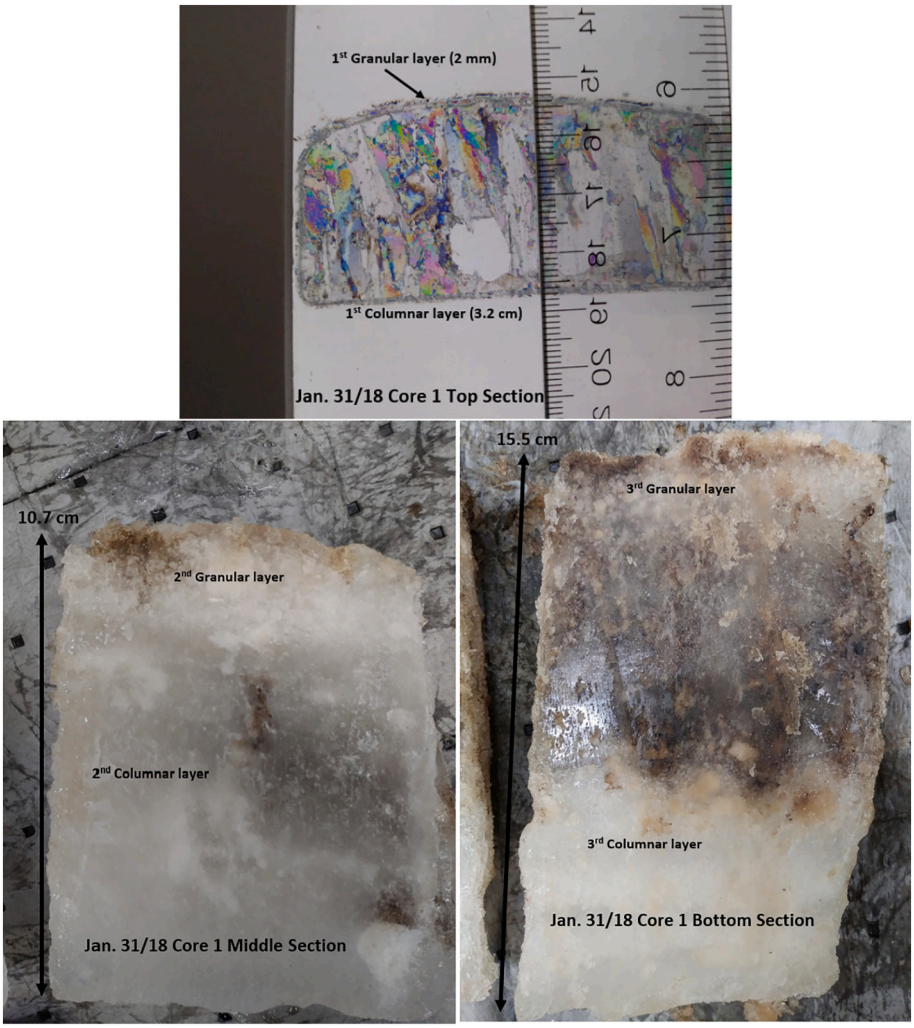

Fig. 1. Example photos of thick sections and a thin section of sea ice from an oil-in-ice mesocosm depicting alternating granular and columnar layers (Desmond et al., 2021).

2.2. Preparation of the X-ray samples before scanning

X-ray samples were carefully cut with a boning saw into either cylindrical or rectangular prism sections, with 3 cm diameters/widths and 2-3 cm heights, from the top and middle sections of 10 separate oil-contaminated ice cores from the 2016-2018 experiments. These subsections were then stored in a freezer at -20 °C until ready for μ-CT analysis. A list of the investigated X-ray samples, their correspondent ice

Table 1
In situ μ-CT sea ice characteristics pertaining to a subset of the X-ray samples.

Ice core ID	Inferred ice type	Ice core section ice depth (cm)	Chamber temperature (°C)	Bulk Salinity (psu)	% brine volume[a]	Oil volume (mL)[b]
Mar. 1/16 Core 8 Top	Frazil (transitional)	0 to 2.3	-14.8	7.4	2.8	<0.01
Mar. 1/16 Core 10 Middle	Frazil (transitional)	5 to 7	-14.8	5.7	2.2	0.30
Feb. 10/17 Core 9 Top	Frazil (transitional)	0 to 2.9	-14.8	12.4	4.8	0.07
Feb. 10/17 Core 9 Mid	Frazil (transitional)	5 to 7.8	-14.8	10.6	4.1	0.30
Mar. 14/17 Core 16	Pancake (transitional)	0 to 3	-14.8	18.0	6.9	0.03
Feb. 7/18 Top Site 3 Core 1	Frazil (transitional)	0 to 2.8	-14.8	5.96	2.3	0.15
Feb. 7/18 Middle Site 3 Core 1	Frazil (transitional)	7.6 to 10.6	-14.8	8.6	3.3	0.25
Feb. 7/18 Middle Site 3 Core 2	Frazil (transitional)	8.8 to 11.3	-14.8	12.6	4.9	<0.01
Feb. 26/18 Top Site 3 Core 3	Frazil (transitional)	0 to 2.4	-14.8	2.0	0.8	0.15
Feb. 26/18 Top Site 3 Core 3	Frazil (transitional)	0 to 2.4	-9.9	2.0	1.1	0.15
Mar. 16/18 Top Site 3 Core 2	Frazil (transitional)	0 to 2.8	-14.8	2.7	1.0	0.25
Mar. 16/18 Top Site 3 Core 2	Frazil (transitional)	0 to 2.8	-9.8	2.7	1.5	0.25
Mar. 16/18 Top Site 3 Core 2	Frazil (transitional)	0 to 2.8	-5.4	2.7	2.6	0.25
Mar. 16/18 Middle Site 3 Core 2	Frazil (transitional)	10.4 to 13.2	-4.7	1.8	2.0	0.30

[a] % brine volume derived from Frankenstein and Garner, 1967.
[b] Oil volume experimentally determined according to Section 2.3.

core depth, and their physical properties (see Sections 2.3 and 2.4.3) are provided in Table 1.

The μ-CT scanning of the samples took place at different temperatures (-15 °C, -10 °C, -6 °C, -5 °C, and -4.8 °C, see Table 1). Prior to X-ray analysis, each sample previously stored at -20 °C was left inside a temperature controlled cold room for 24-h at the intended scanning temperature (Table 1). In order to mimic the natural heat flux from the ocean to the atmosphere, allowing brine inclusions to expand along the vertical direction (z-axis), each X-ray sample was placed on a metal plate with their sides encased in Styrofoam (Fig. 2). After 24 hour equilibration in the temperature-controlled room, the entire sample reached the targeted scanning temperature.

2.3. Experimentally determined volume fractions

After μ-CT analysis, each sub-sectioned X-ray sample was melted inside their respective polypropylene tube at room temperature. Each melted X-ray sample was then measured volumetrically using a graduated cylinder. The crude oil was then separated from the melted sea ice using a Vortex Mixer (VWR) and Hexanes (Fisher Scientific, Optima Grade) as solvent. The collected oil fractions were placed inside a new polypropylene tube and concentrated by fully reducing the solvent to dryness through natural room temperature evaporation. The volumes of the remaining oil samples were then measured by placing an empty polypropylene tube adjacent to the oil filled tube and filling it with known amounts of water, using 10-100 μL pipettes, until both volumes were level with one another. The validity of this method was checked through a blind test using water, in a separate polypropylene tube, to measure known amounts of crude oil. The results of this blind test are shown in Table 2, in which all volumes were found to be accurately measured.

Table 2
Results of blind test assessing accuracy of method used to experimentally measure the oil volumes of the X-ray samples. Note 'true volume' pertains to known amounts of crude oil placed inside polypropylene tubes.

Trial #	True V (mL)	H_2O (mL)
V1	0.9	0.9
V2	0.5	0.5
V3	0.2	0.2
V4	0.09	0.08
V5	0.05	0.04
V6	0.02	0.02

2.4. Analysis by Micro-Computed Tomography (μ-CT) X-ray

2.4.1. Scanning

A Bruker SKYSCAN 1174 Compact Micro-CT system was placed inside a temperature controlled cold room (held at -15/-10/-6/-5/-4.8 °C according to Table 1) and used to analyze sea ice microstructure. Scanning at temperatures warmer than -4.5 °C resulted in degradation of the samples by surface melt. Thermocouples were placed inside the μ-CT sample chamber to record the in-situ ice temperature during scanning (Fig. 3) and typically read +0.2 °C relative to the ambient condition when the X-ray source was on. Samples were placed in polypropylene tubes (Fig. S2), mounted on a rotating stage in the μ-CT (Fig. 3), and rotated a full 180°, in 0.4° increments, averaging frames of 4, with the μ-CT running at 50 kV and 800 μA. An aluminum filter (0.50 mm) was placed in front of the X-ray source during the scan. Individual scans took approximately 3 h. The final image contained 1304 × 1024 pixels with a pixel size and slice thickness of 29 μm. After the scan, the projected radiograph was reconstructed into two-dimensional grayscale slices stacked in the z-direction (corresponding to the vertical direction of the original ice core) using Bruker software (NRecon). During the reconstruction step, each voxel was assigned a grayscale value between 0 and 255 corresponding to a CT value. A CT value is expressed in Hounsfield Units (HU), representing the degree of X-Ray attenuation, whereby denser materials and higher atomic numbers result in greater X-ray attenuation (Duliu, 1999). Data reconstruction also included the removal of ring-artifacts, beam-hardening, post-alignment and Gaussian smoothing to reduce the noise (i.e., Ketcham and Carlson, 2001).

2.4.2. Image processing

For any quantitative or qualitative result derived from a binary image, the most crucial step in the imaging technique is the proper segmentation of the grayscale image into individual windows or phases (e.g., oil, air, brine). In this study, the segmentation process consists of finding the CT-Value, a digital number between 0 and 255, for the ice matrix, the brine, air, and oil inclusions. Optimal thresholds can be determined by eye or automatically based on information contained in the image histogram (Iassonov et al., 2009; Sezgin and Sankur, 2004).

Since air, brine and ice are mediums with different densities, they are easily distinguished by CT X-ray. To distinguish the air and brine from the ice matrix we used the histogram-based method called CL-Otsu (Crabeck et al., 2016; Iassonov et al., 2009) which separated the background (i.e. ice) and foreground voxels (i.e. air/brine) by approximating the histogram with a combination of two or more statistical distributions. The results of each segmentation method were visually evaluated by comparing the raw and segmented images. Finally, the volume fractions of the ice, brine, and air were quantified based on the selected thresholds.

2.4.2.1. Enhanced imaging of oil. Ice and oil have similar CT-values due to their similar density, rendering oil inclusions hardly detectable by the human visual system. Both manual and automated histogram-based threshold selections fail to differentiate these two phases from one another. To identify the CT- oil signature in sea ice, we analyzed two test samples (Fig. 4A and B) with a known volume of crude oil and corn oil in pure ice (i.e., ice formed from distilled water) with the CT. For the first test sample (Fig. 4A), a vertically downward hole (3.75 mm diameter)

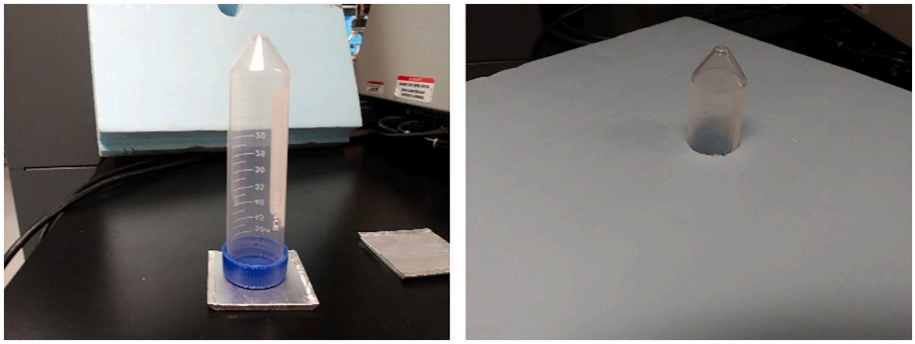

Fig. 2. Example of how X-ray samples were placed on a metal plate and encased in styrofoam prior to placement inside the μ-CT chamber for scanning.

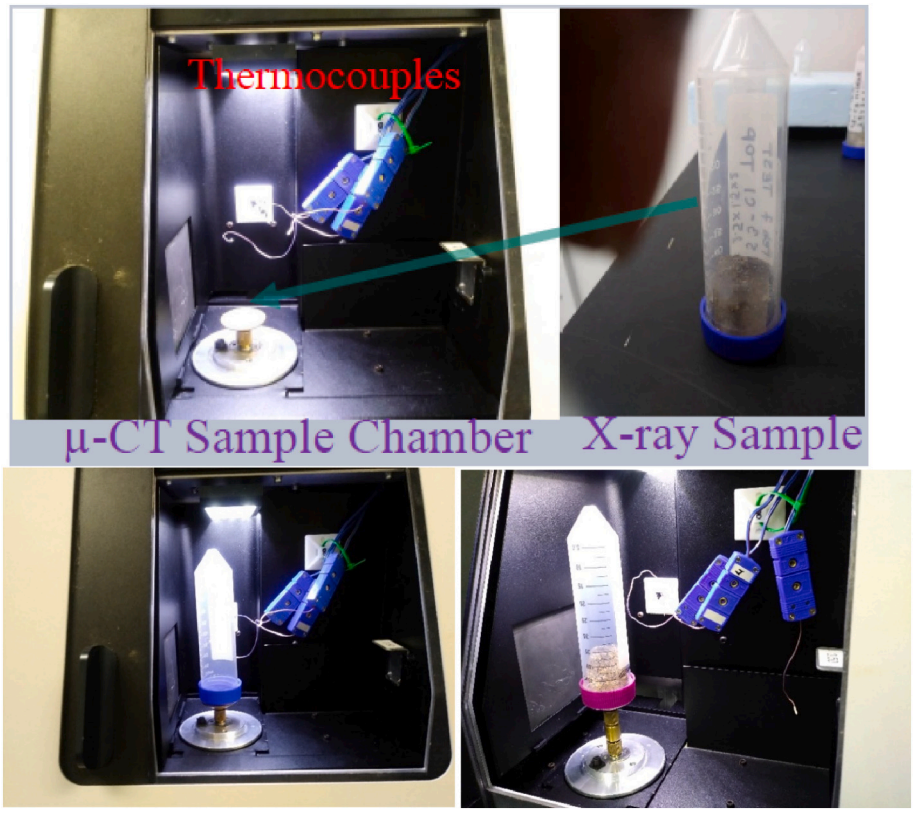

Fig. 3. Sub-sectioned X-ray sample placed inside a polypropylene Falcon tube and subsequently mounted on a rotating sample stage within the μ-CT chamber with installed thermocouples.

was drilled in a cylindrical section of pure ice (2.3 cm height × 2.1 cm diameter) and 120 μL of Tundra crude oil was injected into the hole with a micropipette. Similarly, for the second test sample (Fig. 4B), two vertically downward holes were drilled in a cylindrical section of pure ice in which 100 μL of Mazola corn oil was injected into the right cavity and 50 μL of Tundra crude oil was injected into the left cavity. The spiked samples were then analyzed inside the μ-CT chamber with the use of a polypropylene tube (Falcon, Corning).

As shown in Fig. 4A and B, we can visually distinguish the oil from the other components (i.e., air and ice). Furthermore, the CT-value of the crude oil was observed to be very similar to the polypropylene tube used to hold the sample. The density of polypropylene is known to be 860 kg/m^3 and the crude oil used in our experiments had an initial density of 855 (8) kg/m^3 (Desmond et al., 2019c). Fig. 4D shows the CT-values between the crude oil and the polypropylene tube over the index range of 120-150 and 106-136, respectively. While their respective CT-values are similar to one another, the crude oil CT-values are 10% to 15% higher.

A sea ice sample (Feb. 7 Mid S3C1) (Table 1), taken during the 2018 oil-in-ice mesocosm experiment, was sub-sectioned for analysis by μ-CT and placed in a polypropylene tube (Fig. 5A). Observation of the constructed histogram (Fig. 5B) shows that it is difficult to detect dispersed oil due to the overwhelming ice volume fraction. The polypropylene tube was used as a "benchmark" for the oil index location, keeping in mind that the Tundra crude oil has a slightly higher CT-value (Fig. 4D); that is, the CT-signature of the polypropylene tube was used as a segmentation threshold allowing for an enhanced detection of oil in sea ice. This allowed for an easier assignment of the proper CT-value signature of the ice matrix and oil inclusions. It is important to note that the ranges of CT-value for the different media are not constant from sample to sample (e.g., Figs. 4D, 5B, Table 3). Consequently, great care must be taken in choosing appropriate thresholds for each respective sample. The human visual system was also used to verify the selection of accurate thresholds (CT-values) (e.g., Fig. 5C) by inspecting a variety of oil inclusions in different sample slices.

From these results, we can infer that it is possible to detect a dispersed amount of oil. Encasing the ice with a material possessing a similar density to that of the oil of interest allows for a magnified imaging of the oil inclusions within the sea ice microstructure and the selection of a proper segmentation threshold.

2.4.3. Threshold optimization

A source of error that exists while processing a CT X-ray image occurs during the selection of thresholds due to a lack of knowledge of the optimal segmentation result. To verify the validity of the thresholds for brine, CT-derived brine volumes were compared to brine volumes computed using the state equations of Frankenstein and Garner (1967). Frankenstein and Garner (1967) state equations use in-situ temperature (here CT-chamber temperature) and bulk ice salinity to compute the brine and ice volume fractions. Bulk ice salinities of each X-ray sample were measured with a conductivity meter (Orion Star A212 – Thermo Scientific) on the collected saltwater fractions, previously obtained by separation from the oil. The accuracy of CT-derived fractions (air, brine) and their agreement with values derived from state equations have previously been investigated (Crabeck et al., 2016; Salomon et al., 2017). In case of a mismatch between CT-derived and state equation derived brine and ice volume fractions, the thresholds were adjusted to reach agreement (Table 4). Similarly, the CT-derived oil volume was compared to the experimentally measured oil volume. The threshold was finely adjusted to reach agreement if the CT-derived oil volume mismatched the experimental oil volume (Table 4).

A second source of error is linked to the resolution of the CT-image which is always insufficient to resolve every object and its boundary. When an inclusion is smaller than the spatial resolution of the image, it appears as a mixed pixel. In this study, the major source of mixed pixels is at the boundary of ice and air (e.g., in air pockets) resulting in an

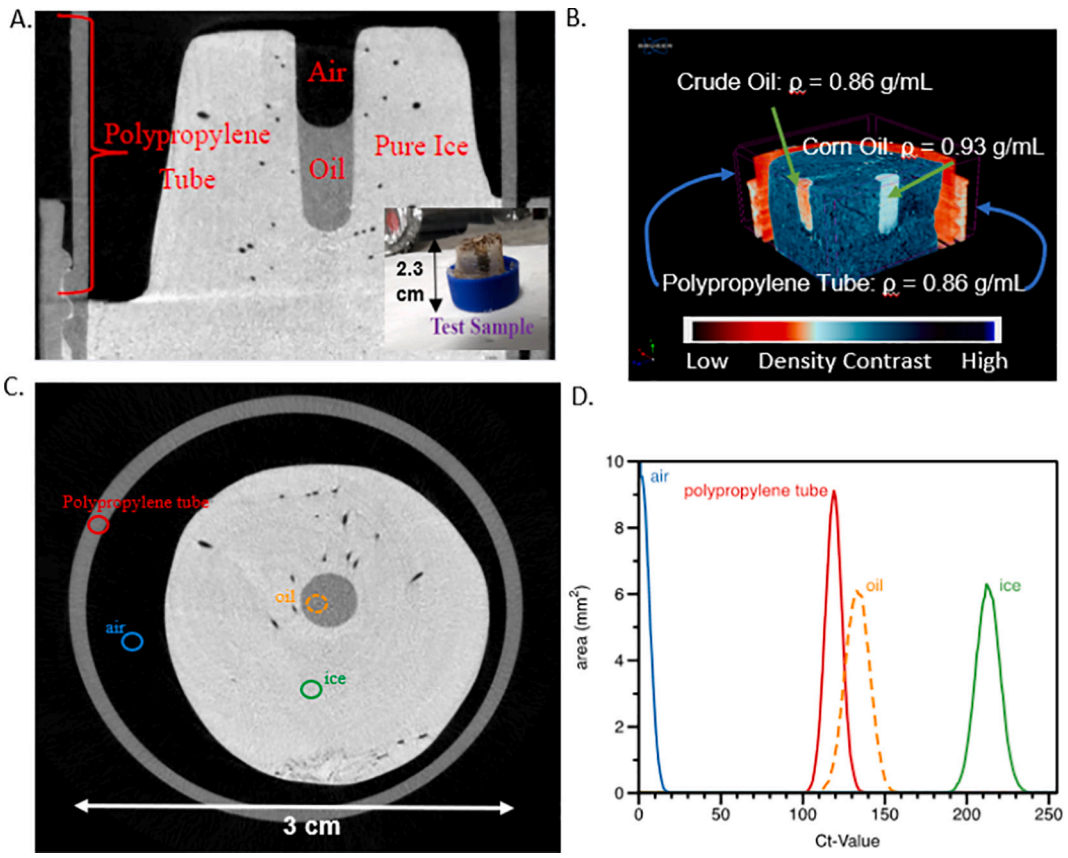

Fig. 4. Panel A shows a raw transversal in the XZ direction of a test sample contained in a polypropylene tube in which crude oil was injected. Panel B shows a second test sample contained in a polypropylene tube in which both crude and corn oil was injected. The density contrast of the different medium (ice, crude oil, corn oil and polypropylene tube) are shown in the color bar. Panel C shows a transversal slice of the test sample in panel A. Panel D shows a CT histogram of the medium highlighted in panel C. The histogram combined the data over a stack of 147 slices. (For interpretation of the references to color in this figure legend, the reader is referred to the web version of this article.)

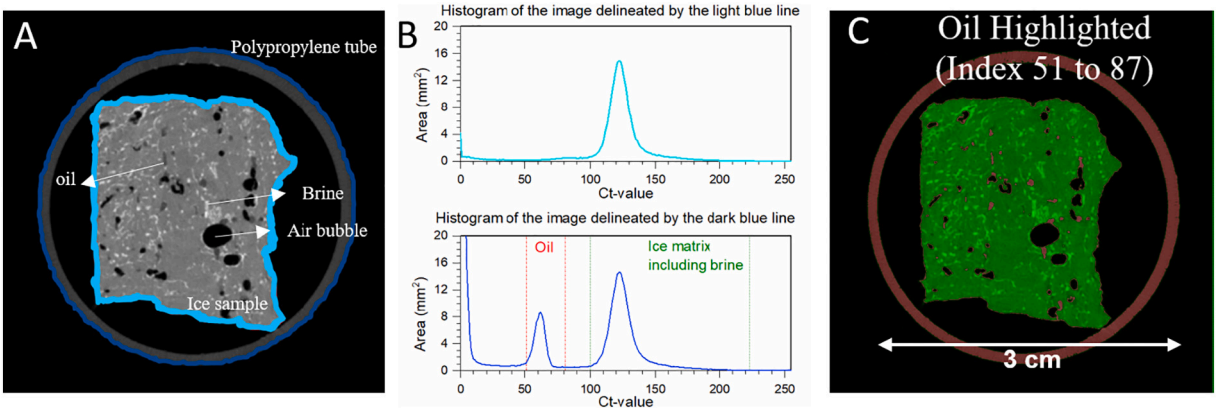

Fig. 5. Panel (A) shows a raw transversal slice of an oil-contaminated ice sample (Feb. 7/18 Middle S3C1) contained in a polypropylene tube. In this image, brine appears in white and very light grey, air bubbles appear in black, and oil inclusions appear in dark grey. Panel (B) shows histograms delineating the light blue and dark blue lines shown in the panel A image. Panel (C) shows the ice matrix in green, and the oil and polypropylene tube pixels in red, selected using the Ct-value of oil from the panel B histogram. (For interpretation of the references to color in this figure legend, the reader is referred to the web version of this article.)

averaged CT-value similar to that of the Tundra crude oil, which can lead to a false positive of oil volume. This source of error is minimized while X-ray samples contain appreciable volumes of oil. In this study, we focused our analyses on samples which contained ≥150 μL oil or 2.14% oil/ice vol (Table 1), which reduced the impact of false positives on the CT-derived volume. The human visual system was also used to verify the selection of accurate thresholds (CT-values) by inspecting and comparing several individual inclusions and their boundaries on raw and segmented images.

2.5. Proximity of oil and brine inclusions analysis

To quantify the extent of boundary overlap or interface connection between the oil and brine inclusions, the segmented brine and oil

Table 3
Averaged (stdev) 3D individual object analysis of sphericity and structure model index (SMI) for a subset of 2015-2018 X-ray samples.

Sample (ambient T)	Media (CT thresholds)	Sphericity	SMI
Mar. 1/16 C10 Mid (-15 °C)	Oil (80-120)	0.75 (15)	2.74 (62)
	Air (0-57)	0.75 (12)	2.86 (35)
	Brine (178-255)	0.78 (10)	2.93 (25)
Feb. 10/17 C9 5-7.5 cm (-15 °C)	Oil (60-94)	0.71 (17)	2.57 (63)
	Air (0-27)	0.74 (13)	2.78 (37)
	Brine (182-255)	0.74 (11)	2.81 (25)
Feb. 7/18 Top S3C1 (-15 °C)	Oil (121-148)	0.69 (16)	2.50 (40)
	Air (0-74)	0.72 (14)	2.68 (40)
	Brine (242-255)	0.77 (11)	3.00 (25)
Feb. 7/18 Mid S3C1 (-15 °C)	Oil (62-87)	0.71 (17)	2.52 (56)
	Air (0-41)	0.72 (15)	2.63 (41)
	Brine (167-255)	0.79 (11)	3.09 (28)
Feb. 7/18 Mid S3C2 (-15 °C)	Air (0-35)	0.68 (46)	2.87 (47)
	Brine (170-255)	0.77 (11)	2.97 (28)
Feb. 26/18 Top S3C3 (-15 °C)	Oil (81-107)	0.70 (17)	2.49 (56)
	Air (0-48)	0.72 (15)	2.60 (40)
	Brine (167-255)	0.79 (09)	2.95 (25)
Feb. 26/18 Top S3C3 (-10 °C)	Oil (86-119)	0.72 (18)	2.55 (70)
	Air (0-48)	0.71 (15)	2.58 (41)
	Brine (175-255)	0.79 (09)	2.96 (24)
Feb. 26/18 Top2 S3C3 (-5 °C)	Air (0-53)	0.72 (14)	2.63 (42)
	Brine (189-255)	0.78 (10)	2.87 (25)
Mar. 16/18 Top S3C2 (-15 °C)	Oil (67-107)	0.74 (17)	2.66 (69)
	Air (0-43)	0.73 (15)	2.72 (46)
	Brine (166-255)	0.78 (10)	2.93 (24)
Mar. 16/18 Top S3C2 (-10 °C)	Oil (71-107)	0.68 (22)	2.37 (96)
	Air (0-47)	0.75 (14)	2.76 (42)
	Brine (171-255)	0.78 (10)	2.96 (24)
Mar. 16/18 Top S3C2 (-6 °C)	Oil (76-110)	0.77 (13)	2.80 (55)
	Air (0-49)	0.73 (14)	2.67 (41)
	Brine (155-255)	0.73 (14)	2.95 (25)
Mar. 16/18 Mid S3C2 (-4.8 °C)	Oil (87-114)	0.70 (17)	2.49 (59)
	Air (0-43)	0.74 (15)	2.75 (50)
	Brine (189-255)	0.77 (11)	2.93 (25)
Total average	Oil	0.72 (17)	2.57 (63)
	Air	0.73 (17)	2.71 (42)
	Brine	0.77 (11)	2.95 (25)

Total average is the average of all average (stdev) values above for the oil, air, and brine inclusions respectively.

Table 4
Comparison of CT-derived and experimentally determined volumes for the media of brine, pure ice, and crude oil for sea ice sample "Feb. 7/18 Middle S3C1" (see Table 1 and Fig. 5).

Media	CT-derived volume (mL)	Experimental volume (mL)
Brine (index 167-223)	0.264	0.265
Pure ice (index 100-167)	7.539	7.400
Crude oil (index 62-87)	0.198	0.200

components for each respective horizontal slice (XY-plane) of three representative X-ray samples were exported as individual PNG images.

$$\Psi spheroid = \frac{\pi(w)^{\frac{2}{3}}}{2\int_0^{\pi/2}\int_0^{\pi/2} wcos\varphi\sqrt{sin^2\varphi + cos^2\Theta cos^2\varphi + \left(\frac{1}{w^2}\right)sin^2\Theta cos^2\varphi}\,d\varphi d\Theta} \quad (2)$$

Images were processed in MATLAB 2020a to determine the pairwise pixel overlap and fraction of interface connection between horizontal slice pairs of oil and brine. A percentage of boundary overlap between the oil and brine was calculated based on the overlap of pixels from the oil and brine inclusions from each image set. The overlap percentages obtained for each horizontal slice of the representative X-ray samples were then displayed as box plots for oil-brine overlap. Interface connection was determined using a function to check pixels bordering a pixel of interest in both lateral and diagonal directions, calculated as a percentage over the calculated perimeter of the feature being checked against. For example, the interface percent between brine and oil was calculated by determining the total oil pixels bordering all brine pixels, and dividing the resulting value by the total perimeter or border of all brine features. These results were used to help assess the potential for bioremediation of oil in sea ice.

2.6. Individual object analysis of sea ice inclusions

The geometry, orientation, and size of the sea ice inclusions (i.e., oil, air, and brine) were determined from quantitative analysis of the x- ray microtomography scans. Averaged (standard deviation) 3D Individual Object Analyses (IOA) of sphericity (Ψ), structure model index (SMI), orientation (theta), and major diameter were conducted for a subset of the 2015-2018 X-ray samples. *Sphericity* (Ψ) is a measure of how spherical a 3D object is, with an index ranging from 0 to 1 (perfect sphere). This parameter is defined by (Wadell, 1935). SMI indicates the relative prevalence of rods and plates in a 3D structure and involves a measurement of surface convex curvature (Hildebrand and Rüegsegger, 1997). An ideal plate, cylinder and sphere have SMI values of 0, 3 and 4, respectively. A structure between the ideal state of a plate and cylinder will have a SMI value between 0 and 3. *Orientation (theta)* is defined as the angle of an individual 3D object oriented between 0° (horizontal XY-plane) and 90° (vertical Z-plane). For instance, an ellipsoid with an angle theta equal to 90 degrees would have its major axis along the vertical z-direction, and an angle theta equal to 0 degrees would correspond to an ellipsoid with its major axis within the XY-Plane. *Major diameter* is the distance between the two most distant pixels in a 3D object. The calculated parameters of sphericity (Ψ), SMI, orientation (theta), and major diameter are tabulated for a subset of the investigated X-ray samples (Table 3). Inclusions with a size similar to the spatial resolution of the image were excluded from the statistical analyses provided in Table 3. When the inclusion has the size of a pixel, it means that the inclusion is smaller than the pixel and that the spatial resolution of the CT-image is insufficient to characterize its geometry.

Specifically, the calculated orientations were used to assess the randomness or degree of vertical alignment of oriented inclusions as a means of assessing sea ice type (granular, columnar). Major diameters of each inclusion type were calculated to determine the size of their features. Sphericity (Ψ) and SMI were used to infer the geometry of inclusions in conjunction with Eqs. (1)–(2) (Li et al., 2012).

$$\Psi cylinder = \frac{(1.5w)^{\frac{2}{3}}}{w + 0.5} \quad (1)$$

where Ψ – sphericity (as defined above); w – aspect ratio of the height (z-direction) divided by the major axial length (XY-plane).

2.7. Remote sensing modelling: application of inclusion geometry analysis

To demonstrate the use of the inferred inclusion geometry to a remote sensing application, we incorporated our results in a modelling study on the Normalized Radar Cross-Section (NRCS) of sea ice based on physical measurements (Desmond et al., 2019b) and compared to experimentally determined NRCS (Neusitzer et al., 2018a; Firoozy et al., 2018). Wave scattering and consequently the electromagnetic footprint of the profiles measured by satellite or on-site radar systems are related to the incidence angle, surface roughness, volume fractions of all the components of sea ice (ice, brine, air, oil), and permittivity (dielectric) profile including real and imaginary parts (Ulaby and Long, 2014). Generally speaking, the brine volume fraction has the greatest impact on the NRCS of the sea ice, assuming the incidence angle remains constant. The equivalent permittivity of a complex material such as sea ice is related to the complex permittivity (dielectrics) of the individual substances, their volume fractions, their spatial distributions, and their orientations relative to the direction of the incident electric-field vector. The substance with the highest volume fraction is regarded as the host material, or continuous medium, and the other substances are regarded as inclusions (Ulaby and Long, 2014). Popular dielectric mixture formulas for heterogenous materials include the Tinga-Voss-Blossey (TVB) (Ulaby and Long, 2014; Tinga et al., 1973) and Polder–van Santen/de Loor (PVS) (Ulaby and Long, 2014; Polder and van Santen, 1946; De Loor, 1968) models. These models consider the inclusions to be ellipsoidal particles of identical shape and size, randomly oriented with respect to the direction of the electric field of the incident wave. Variations of ellipsoidal particles include 1) prolate spheroid with $x = y$ (symmetric about the z-axis) and $z > x$; 2) sphere with $x = y = z$; 3) oblate spheroid with $x = y$ and $z < x$; 4) circular disk inclusions for thin circular disks with $x = y$ and $z \ll x$; and 5) needle inclusions for long, narrow needles with $x = y$ and $z \gg x$. Herein, we model and compare the sea ice inclusions as circular disks (based on the results of our inclusion geometry analysis).

2.7.1. Modelling approach

The Normalized Radar Cross-Section (NRCS) of the sea ice was simulated from the complex permittivity profiles of the physical samples collected throughout the experiment (Desmond et al., 2019b) (Table 5). The permittivity profiles of the ice were modelled at 5.5 GHz using the quasi two-phase Tinga-Voss-Blossey (TVB) and Polder–van Santen/de Loor (PVS) mixture models following (Neusitzer et al., 2018a; Firoozy et al., 2018). The PVS and TVB model assumes that the mixture is comprised of randomly oriented inclusions (e.g., oil, air, brine) surrounded by the host material (i.e., pure ice). In this formulation, the inclusions are considered to be separate within the host material. The Integral Equation Model (I^2EM) (Fung et al., 2002; Ulaby and Long, 2014) was utilized to simulate the monostatic NRCS of the sea ice from the modelled dielectric profiles. As the I^2EM assumes a half-space with a rough interface, the permittivity profiles were reduced to an effective permittivity as a half-space by taking the first 2.5 cm of the modelled dielectric depth profiles based on their calculated NRCS penetration depth (Ulaby and Long, 2014) (Tables 6 and 7). Simulations were run at the same frequencies and incidence angles as the experimental conditions seen in (Neusitzer et al., 2018a; Firoozy et al., 2017). Relevant root-mean-square (RMS) heights and correlation lengths from Table 8 were used for the roughness parameters of the NRCS simulation. Surface roughness is an integral parameter concerning microwave scattering from sea ice.

Table 6
Calculated NRCS penetration depths (cm) of the circular disk dielectric mixture model of sea ice for various sampling times (Desmond et al., 2019a; Neusitzer et al., 2018a).

Sampling dates	TVB/Circdisc	PVS/Circdisc
Jan. 18/16, 12:00 PM	0.5857	0.5653
Jan. 19/16, 12:00 PM	0.8442	0.8439
Jan. 20/16, 9:00 AM	0.7077	0.6881
Feb. 12/16, 1:15 PM	0.6806	0.6034

Table 7
Calculated effective permittivities "seen" by the I^2EM NRCS model of the circular disk dielectric mixture model of sea ice for various sampling times (Desmond et al., 2019a; Neusitzer et al., 2018a).

Sampling dates	TVB/Circdisc	PVS/Circdisc
Jan. 18/16, 12:00 PM	7.1584–4.1153i	7.3169–4.3180i
Jan. 19/16, 12:00 PM	5.4315–2.4542i	5.4230–2.4534i
Jan. 20/16, 9:00 AM	6.2074–3.1475i	6.2991–3.2650i
Feb. 12/16, 1:15 PM	7.3223–3.5459i	7.7769–4.1435i

Table 8
RMS heights and correlation lengths (L) of relatively smooth and rough ice obtained using LiDAR.

	Observed ice characteristics	RMS height (cm)	Stdev (cm)	L (cm)
Firoozy et al., 2018	Smooth ice, no accumulation	0.261	0.001	0.307
Firoozy et al., 2017	Frost flowers, small snow grains	0.39	0.088	0.965

Stdev is the standard deviation of RMS height.

3. Results and discussion

3.1. Qualitative analysis

3.1.1. Oil behaviour and movement tendencies in sea ice: oil distribution and location

Horizontal/vertical cross-sections of the samples were obtained through X-ray imaging and are shown in Figs. 5A, 6, S3–S4. These cross-sections illustrate oil distribution within the ice, indicating that the oil included within the ice was quite dispersed and tended to surround the perimeter of air inclusions. Many exclusive pockets of oil were also observed. Further observation of these figures shows that the brine was separate from the oil within the ice, with minimal interface contact. This

Table 5
Comparisons between modelled and experimental NRCS (dB) for various sampling times (Desmond et al., 2019a; Neusitzer et al., 2018a).

Sampling dates	Ice conditions		Surface roughness inputs (cm)	Incidence angle (°)	Experimental	TVB/ Circdisc	PVS/ Circdisc
Jan. 18/16 12:00 PM	Relatively rough	Full bloom, small snow grains	rms = 0.39, L = 0.965	56°	-7.52	-9.80	-9.66
Jan. 19/16 12:00 PM	Relatively rough	Full bloom, small snow grains	rms = 0.39, L = 0.965	56°	-9.52	-11.50	-11.50
Jan. 20/16 9:00 AM	Relatively rough	Full bloom, small snow grains	rms = 0.39, L = 0.965	56°	-8.36	-10.65	-10.55
Feb. 12/16 1:15 PM	Relatively smooth	No accumulation	rms = 0.261, L = 0.307	57°	-20.78	-21.60	-21.20

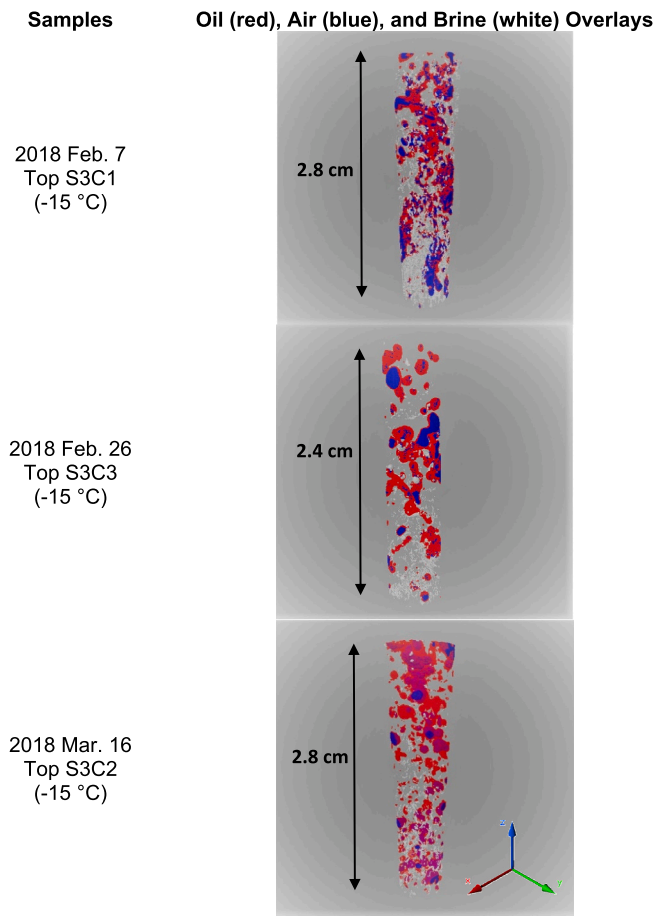

Fig. 6. The 3D decomposition of top sections of sea ice cores from SERF 2018 in which oil, air, and brine are represented in red, blue, and white respectively. (For interpretation of the references to color in this figure legend, the reader is referred to the web version of this article.)

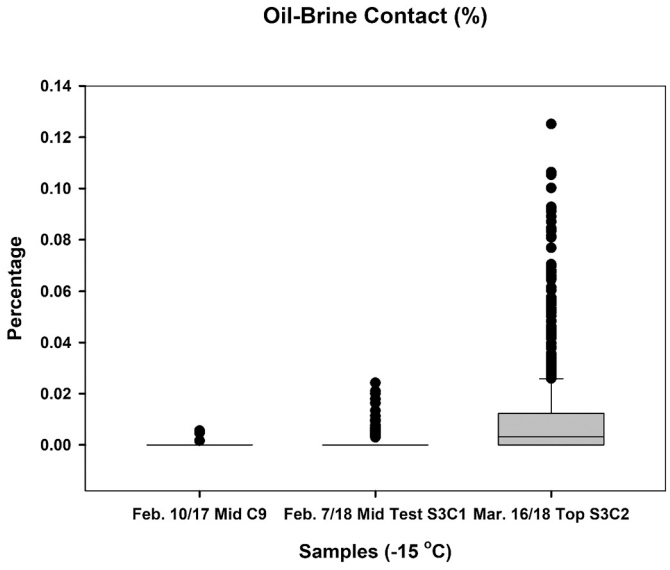

Fig. 7. Percentage of oil and brine boundary overlap (interface connection) for a subset of X-ray samples.

result is likely due to the natural separation of oil and water owing to differences in density and hydrophobic character; that is, the oil percolated through brine channels progressively pushing out and replacing the brine, and subsequently the oil became encapsulated within the ice (Petrich et al., 2013; Maus et al., 2015; Desmond et al., 2019a; Saltymakova et al., 2020). From Figs. 6 and S4, most oil accumulation is observed towards the top of each X-ray sample, respectively. In these areas of high oil concentration, less brine is present in contrast to the bottom of each sample which is richer in brine. This separation of brine is further demonstrated by Fig. 7, in which the average interface contact percentage between the brine and oil for the investigated X-ray samples was calculated to be less than 0.13%. It is worth noting that the samples investigated in Fig. 7 were analyzed by μ-CT at -15 °C. It is expected that oil-brine contact would increase at warm temperatures approaching 0 °C. However, due to the resolution limitations of the μ-CT instrument at warm temperatures and the possibility of sample melt during scanning, we were unable to extensively investigate samples at warmer temperatures.

3.1.2. Mitigation potential

Based on the aforementioned 2015-2018 oil-in-ice mesocosm experiments, the bulk of the oil was found to be encapsulated in the upper layers of the sea ice (Desmond et al., 2019a, 2019b, 2019c, 2021; Saltymakova et al., 2020), separate from the brine (Figs. 5A, 6–7, S3–S4). Brine and seawater are the media in which oil-degrading bacteria can thrive, containing the essential nutrients required to catalyze the biodegradation reaction (Vergeynst et al., 2018; Boetius et al., 2015; Prince and Walters, 2016). Significant biodegradation can only result when the bulk of the oil is in direct contact with brine or sea water, such as at the base of the sea ice or in the presence of a melt pond (Vergeynst et al., 2018). The fact that oil remains separate from brine and attempts to concentrate towards the surface may act to decrease the likelihood of microbial bacteria from interacting with the surfaced oil, as there is a larger bacterial population towards the sea ice base and within brine compared to vacant ice interstices (Boetius et al., 2015; Boccadoro et al., 2018). However, under warm ice temperatures (i.e., ≥ -5 °C), there is greater potential for active brine to be in physical contact with or adjacent to oil surrounding ice interstices owing to the large increase and expansion of brine (Eicken, 2003; Petrich and Eicken, 2010); this may allow for a partial degradation of the bulk oil encapsulated within surficial ice.

Dissolution of lighter oil concentrations in brine (Saltymakova et al., 2020; Desmond et al., 2019b; Payne et al., 1991b), containing oil-degrading bacteria (Brakstad et al., 2008; Delille et al., 1997), may show greater potential for bioremediation of crude oil in the Arctic. The lighter fractions of crude oil are known to be toxic to marine life (Anderson et al., 1974), and the success of its bioremediation will be crucial in the case of an oil spill. We expect that bioremediation will effectively grow with a decrease in the concentration of crude oil in the ice as the dissolution efficiency increases (Saltymakova et al., 2020; Desmond et al., 2019b). We also expect that the bulk oil encapsulated in the ice to be less weathered in comparison to open water (Saltymakova et al., 2020; Desmond et al., 2021), and will be prone to biodegradation during the spring-summer season, when the oil can come into direct contact with the ocean (Martin, 1979).

3.2. Quantitative analysis

3.2.1. Orientation, size, and geometry of inclusions

Based on the 3D IOA, all inclusions were found to be somewhat randomly oriented within the samples with orientation angles theta ranging from 0 to 90° (Fig. 8c). Air bubbles and oil inclusions show two modes (0 and 90°), while brine shows a very slight 90° mode and is more

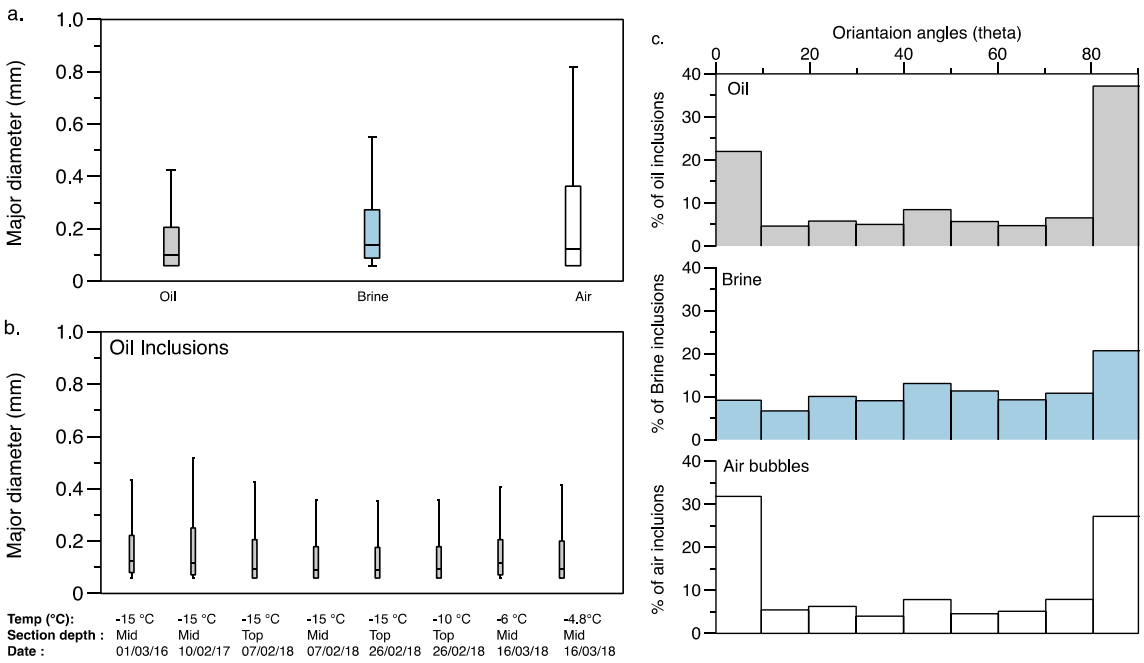

Fig. 8. The panel (a) shows IQR box plot for the distribution of CT-derived major diameter of all oil, brine and air inclusions analyzed. The panel (b) shows IQR box plot for the distribution of CT-derived major diameter of oil inclusions for various samples from the different experiment (2016, 2017, 2018). The box is defined by the first and third quartiles of the distribution, the line in the box is the median. The panel (c) shows the histogram of the orientation angles (theta) for all the oil, brine and air inclusions analyzed.

pronouncedly defined by random orientation (typical of granular ice) (Eicken, 2003; Galley et al., 2015).

Based on the calculated major diameters of all inclusion types, feature sizes for all three of the artificial oil-in-ice mesocosm experiments (Section 2.1) were less than 1 mm (Fig. 8a and b). The majority of brine inclusions analyzed have a major diameter ranging from 0.1 to 0.3 mm. Similarly, Lieblappen et al. (2018) reported brine structure thicknesses of less than 0.2 mm. Air inclusions have a larger range of diameter with 75% of the air bubbles having diameters smaller than 0.4 mm. Fig. 8b shows the distribution of CT-derived major diameters of oil inclusions for various samples. From this figure we see that 1) the size of the oil inclusions was similar during the different experiments (2016, 2017, 2018), 2) sea ice temperature did not impact the size of the oil inclusions, 3) the inclusion size of oil does not vary with depth (top and middle sections are the same), and 4) more than 25% of the oil inclusions were smaller than 0.1 mm, and only 25% were larger than 0.2 mm.

The CT-derived sphericities of the oil, air, and brine inclusions were 0.72 (17), 0.73 (17), and 0.77 (11) on average (stdev), respectively (Table 3). Their typical SMI values were on average (stdev) 2.57 (63), 2.71 (42), and 2.95 (25), respectively (Table 3). Our SMI results for brine are similar to those reported in Lieblappen et al. (2018), who also observed SMI values slightly below 3 for brine pockets. Based on the calculated SMI values, we know that the average inclusion best resembles ideal cylinders, rather than ideal plates or spheres, and that the inclusions are less than ideal (i.e., <SMI = 3). Based on the calculated sphericity values ($\Psi = 0.72, 0.73, 0.77$) we can infer that the inclusions resemble a cylinder of height (h) / diameter (d) = (0.3, 0.3, 0.4) (w) (Eq. (1) (herein); Fig. 1, Li et al., 2012). By definition, a cylinder with h / d < (1 = ideal) is considered a disk.

If we instead consider the average geometry of inclusions to be an oblong ellipsoid (or an oblate spheroid for simplicity), as they appear visually in Figs. 5A, 6, and S3–S4, and in other literature such as (Galley et al., 2015), results in $w = h / d = 0.3$ using $\Psi = 0.75$ (Eq. (2) (herein); Fig. 19, Li et al., 2012).

In either case, whether we consider the average inclusions as a cylinder or more realistically as an oblate ellipsoid, based on the computed sphericity and SMI values, we can conclude that the average inclusion most closely resembles a disk or oblate spheroid of marginal thickness with h / d = 0.3-0.4.

As a means of demonstration, we modelled the dielectrics of the 2016 SERF sea ice (Desmond et al., 2019b) with circular disk inclusions, and subsequently simulated the resultant Normalized Radar Cross-Section (NRCS) from the sea ice dielectrics. The modelled NRCS was then compared with experimental NRCS (see Sections 2.7 and 3.2.2 for more details).

3.2.2. *Remote sensing potential*

Table 5 compares experimental and simulated NRCS, whereby the simulated results correspond to sea ice inclusions modelled as randomly oriented circular disks (Section 3.2.1). All simulated results show a lower NRCS compared to experimental. Ice conditions with no accumulation show the best agreement with less than 1 dB difference. There is comparatively lesser agreement (~2 dB) between experimental and simulated NRCS for ice cover with accumulation; in particular, the presence of fully-developed frost flowers. Reasons for this include 1) the fact that frost flowers have not been studied extensively and are not fully understood (Isleifson et al., 2014), and 2) that brine expulsion during frost flower formation may not have been properly accounted for in the dielectric modelling, as surface ice scrapings were not taken for surface salinity measurements. Instead, the bulk salinity from the first 2.5 cm of each ice core was measured, which may have resulted in a slight systematic decrease in simulated NRCS compared to experimental.

The calculated penetration depth for the circular disk inclusions were found to be surficial and within the 1st cm of the upper sea ice layer (Table 6), which is fitting as the NRCS (I^2EM) model used assumes surface scattering. Furthermore, in a naturally grown sea ice environment such as in the Northern Arctic, significantly thicker layers of granular ice are observed on the surface of sea ice (>5 cm) compared to artificially grown sea ice in microcosm/mesocosm tanks (Galley et al., 2015; Ehn et al., 2007; Isleifson et al., 2010). Consequently, modelling sea ice inclusions as randomly oriented ellipsoidal particles is quite

applicable for airborne sensors which probe the sea ice surface (composed of randomly oriented crystals). Overall, these results suggest that the inclusions of surficial sea ice (granular/inter-granular) can be modelled by the profile of disks.

To confirm our findings, future work should include 1) the measurement of surficial sea ice dielectrics with the use of a dielectric probe for direct comparison with modelled dielectrics; and 2) a more thorough comparison between modelled and experimental NRCS at various incidence angles, incorporating LiDAR measurements corresponding to each physical sampling date. We also note that future studies should involve the modelling of oblate spheroid inclusions. It is important to establish which dielectric model(s) best describe sea ice as it has implications for remotely inferring both the oil type (light, medium, heavy) and magnitude of spilled oil through the use of an inversion algorithm (e.g., Firoozy et al., 2017; Firoozy et al., 2018), allowing for swifter planning of an appropriate mitigation response.

Lastly, based on Section 3.1.1, we know that oil has the tendency to displace and remain separate from brine within surficial sea ice as well as in its depth profile (Figs. 5A, 6–7, S3–S4) (Desmond et al., 2019a; Saltymakova et al., 2020). The lowering of sea ice salinity caused by the oil's presence can result in a reduction of the NRCS and may be eminently detectable in the case of a real-world oil spill (Firoozy et al., 2017; Firoozy et al., 2018).

4. Conclusion

X-ray computed microtomography was used to assess the qualitative and quantitative capabilities for examining oil-contaminated sea ice (granular/inter-granular). Use of polypropylene tubes were found to enhance the capacity for imaging crude oil-in-ice, as they possess a similar density to the crude oil used in this study (~860 kg/m^3). We postulate that polyethylene tubes (960 kg/m^3) would enhance the imaging of heavier crude oils-in-ice. It is worth noting the limitation of our proposed method which requires large quantities of oil in sea ice (e.g., >2.1% oil/ice vol.) to alleviate false positives arising from mixed pixels. Future X-ray work should improve and build on this work.

Through our investigations, oil was found to distribute throughout the ice to an extent and tended to occupy the perimeter of large vacant pockets or completely occupy smaller void pockets and remained separate from the brine. Based on the oil distribution and proximity relative to brine within the upper layers of sea ice, the success of bioremediation is expected to be insignificant for the bulk oil, but would likely be most significant for the lighter and potentially more toxic water soluble oil constituents which dissolved in the brine and became subsequently driven into the water column upon warm conditions. The bulk oil may be preserved within the upper layers of the ice until spring thaw, where it could be potentially biodegraded.

Based on the CT-derived sphericities and SMI values of the sea ice constituents, it was determined that the oil, air, and brine inclusions closely resemble the geometry of an elliptic disk or oblate spheroid. Based on this discovery, standard remote sensing modelling techniques were used to simulate the NRCS of sea ice representing inclusions as circular disks. These simulations were then compared to experimental NRCS, demonstrating the applicability of our modelling approach.

CRediT authorship contribution statement

Durell S. Desmond: Conceptualization, Investigation, Methodology, Formal analysis, Visualization, Writing – original draft, Writing – review & editing. **Odile Crabeck:** Formal analysis, Methodology, Visualization, Writing – original draft, Writing – review & editing. **Marcos Lemes:** Investigation, Methodology, Writing – review & editing. **Madison L. Harasyn:** Formal analysis, Writing – original draft, Writing – review & editing. **Amirbahador Mansoori:** Formal analysis, Writing – review & editing. **Diana Saltymakova:** Visualization, Writing – review & editing. **M. Christopher Fuller:** Writing – review & editing. **Søren Rysgaard:** Funding acquisition, Writing – review & editing. **David G. Barber:** Funding acquisition. **Dustin Isleifson:** Writing – review & editing. **Gary A. Stern:** Project administration, Funding acquisition, Writing – review & editing.

Declaration of competing interest

The authors declare that they have no known competing financial interests or personal relationships that could have appeared to influence the work reported in this paper.

Acknowledgements

Canada Research Chair (CRC) programs, Natural Sciences and Engineering Research Council (NSERC) of Canada, the Canada Foundation for Innovation (CFI) and the University of Manitoba (UofM). This work was supported by and is a contribution to the ArcticNet Networks of Centres of Excellence and the Arctic Science Partnership (ASP), as well as Microbial Genomics for Oil Spill Preparedness in Canada's Arctic Marine Environment (GENICE). We would also like to thank Ryan Galley, Thomas D. Neusitzer, Nariman Firoozy, Katarzyna Polcwiartek, Nolan Snyder, and Dr. Nicolas-Xavier Geilfus (CEOS).

Appendix A. Supplementary data

Supplementary data to this article can be found online at https://doi.org/10.1016/j.marpolbul.2021.112996.

References

AMAP, 2010. AMAP Assessment 2007: oil and gas activities in the arctic — effects and potential effects. Arctic Monitoring & Assessment Programme, Oslo vols. 1 and 2.
AMAP, 2017. Snow, Water, Ice and Permafrost in the Arctic (SWIPA) 2017. Arctic Monitoring and Assessment Programme (AMAP), Oslo, Norway vols. 1 and 2.
Afenyo, M., Khan, F., Veitch, B., Yang, M., 2016a. Modeling oil weathering and transport in sea ice. Mar. Pollut. Bull. 107, 206–215.
Afenyo, M., Veitch, B., Khan, F., 2016b. A state-of-the-art review of fate and transport of oil spills in open and ice-covered water. Ocean Eng. 119, 233–248.
Anderson, J.W., Neff, J.M., Cox, B.A., Tatem, H.E., Hightower, G.M., 1974. Characteristics of dispersions and water-soluble extracts of crude and refined oils and their toxicity to estuarine crustaceans and fish. Mar. Biol. 27, 75–88.
Boccadoro, C., Krolicka, A., Receveur, J., Aeppli, C., Le Floch, S., 2018. Microbial community response and migration of petroleum compounds during a sea-ice oil spill experiment in Svalbard. Mar. Environ. Res. 142, 214–233.
Ballestero, H., Magdol, Z., 2011. Biodegradation of polycyclic aromatic hydrocarbons in simulated arctic sea ice brine channels and protistan predation. In: International Oil Spill Conference Proceedings. https://doi.org/10.7901/2169-3358-2011-1-272 vol. 2011, no. 1.
Bazilchuk, N., 2018. Predicting the fate of oil spills in a frozen world. In: Gemini Research News from NTNU and SINTEF, 15 Feb. geminiresearchnews.com /2018/02/predicting-fate-oil-spills-frozen-world/.
News, B.B.C., 2020. Arctic Circle oil spill prompts Putin to declare state of emergency.. Retrieved from. https://www.bbc.com/news/amp/world-europe-52915807.
Boetius, A., Anesio, A.M., Deming, J.W., Mikucki, J.A., Rapp, J.Z., 2015. Microbial ecology of the crosphere: sea ice glacial habitats. Nat. Rev. Microbiol. 13, 677–690.
Bradford, J.H., Babcock, E.L., Marshall, H.-P., Dickins, D.F., 2015. Targeted reflection-waveform inversion of experimental ground-penetrating radar data for quantification of oil spills under sea ice. Geophysics 81 (1), WA59-WA70.
Brakstad, O.G., Nonstad, I., Faksness, L.-G., Brandvik, P.J., 2008. Responses of microbial communities in Arctic Sea ice after contamination by crude petroleum oil. Microb. Ecol. 55, 540–552.
Brandvik, P.J., Faksness, L.-G., 2009. Weathering processes in Arctic oil spills: meso-scale experiments with different ice conditions. Cold Reg. Sci. Technol. 55 (1), 160–166. https://doi.org/10.1016/j.coldregions.2008.06.006.
Brekke, C., Holt, B., Jones, C., Skrunes, S., 2014. Discrimination of oil spills from newly formed sea ice by synthetic aperture radar. Remote Sens. Environ. 145, 1–14.
Brown, C.E., Fingas, M.F., 2003. Review of the development of laser fluorosensors for oil spill application, 47.9-12 Mar. Pollut. Bull. 477–484. Web.
Courville, Z.R., Lieb-Lappen, R., Claffey, K., Elder, B., 2017. Investigations of skeletal layer microstructure in the context of remote sensing of oil in sea ice. In: Proceedings of the International Oil Spill Conference: Vol. 2017, No. 1, pp. 2237–2255. https://doi.org/10.7901/2169-3358-2017.1.2237.
Cox, G., Weeks, W., 1983. Equations for determining the gas and brine volumes in sea-ice samples. J. Glaciol. 29 (102), 306–316.
Crabeck, O., Galley, R., Dellile, B., Else, B., Geilfus, N.-X., Lemes, M., Roches, M.D., Francus, P., Tison, J.-L., Rysgaard, S., 2016. Imaging air volume fraction in sea ice using non-destructive X-ray tomography. Cryosphere 10, 1125–1145.

Delille, D., Bassères, A., Dessommes, A., 1997. Seasonal variation of bacteria in sea ice contaminated by diesel fuel and dispersed crude oil. Microb. Ecol. 33, 97–105.
De Loor, G.P., 1968. Dielectric properties of heterogeneous mixtures containing water. J. Microwave Power 3 (2), 67–73.
Desmond, D.S., Neusitzer, T.D., Firoozy, N., Isleifson, D., Barber, D.G., Stern, G.A., 2019a. Examining the physical processes of corn oil (Medium crude oil Surrogate) in sea ice and its resultant effect on complex permittivity and normalized radar cross-section. Mar. Pollut. Bull. 142, 484–493.
Desmond, D.S., Saltymakova, D., Neusitzer, T.D., Firoozy, N., Isleifson, D., Barber, D.G., Stern, G.A., 2019b. Oil behavior in sea ice: changes in chemical composition and resultant effect on sea ice dielectrics. Mar. Pollut. Bull. 142, 216–233.
Desmond, D.S., Neusitzer, T.D., Lemes, M.D., Barber, D.G., Stern, G.A., 2019c. Examining the physical interactions of corn oil (medium crude oil surrogate) in sea ice and its potential for chemical partitioning within an Arctic environment. In: Proceedings of the Forty-second AMOP Technical Seminar, Environment and Climate Change Canada, Ottawa, ON, Canada, pp. 66–95.
Desmond, D.S., Saltymakova, D., Smith, A., Wolfe, T., Snyder, N., Polcwiartek, Bautista, M., Lemes, M., Hubert, C.R.J., Barber, D.G., Isleifson, D., Stern, G.A., 2021. Photooxidation and biodegradation potential of a light crude oil in first-year sea ice. Mar. Pollut. Bull. 165, 112154.
Duliu, O.G., 1999. Computer axial tomography in geosciences: an overview. EarthSci. Rev. 48, 265–281.
Eicken, A., 2003. From the microscopic to the macroscopic to the regional scale: Growth, microstructure and properties of sea ice. Contribution to. In: Thomas, D., Dieckmann, G.S. (Eds.), Sea Ice – An Introduction to Its Physics, Biology, Chemistry and Geology. Blackwell Science, London, pp. 22–81.
Ehn, J.K., Hwang, B.J., Galley, R.J., Barber, D.G., 2007. Investigations of newly formed sea ice in the Cape Bathurst polynya: 1. structural, physical, and optical properties. J. Geophys. Res. 112 (C5) (pp. C05 003).
Faksness, L.-G., Brandvik, P.J., 2008. Distribution of water soluble components from Arctic marine oil spills — a combined laboratory and field study. Cold Reg. Sci. Technol. 54 (2), 97–105. https://doi.org/10.1016/j.coldregions.2008.03.005.
Faksness, L.-G., Brandvik, P.J., Daae, R.L., Leirvik, F., Børseth, J.F., 2011. Large-scale oil-in-ice experiment in the Barents Sea: monitoring of oil in water and MetOcean interactions. Mar. Pollut. Bull. 62 (5), 976–984. https://doi.org/10.1016/j.marpolbul.2011.02.039.
Fingas, M., Brown, C.E., 2007. Oil spill remote sensing: a forensic approach. In: Oil Spill Environmental Forensics. Fingerprinting and Source Identification.
Fingas, M.F., Hollebone, B.P., 2003. Review of behaviour of oil in freezing environments. Mar. Pollut. Bull. 47 (9), 333–340.
Firoozy, N., Neusitzer, T., Chirkova, D., Desmond, D., Lemes, M., Landy, J., Mojabi, P., Rysgaard, S., Stern, G., Barber, D.G., 2018. A controlled experiment on oil release beneath thin sea ice and its electromagnetic detection. IEEE Trans. Geosci. Remote Sens. 56 (8), 4406–4419.
Firoozy, N., Neusitzer, T., Desmond, D.S., Tiede, T., Lemes, M., Landy, J., Mojabi, P., Rysgaard, S., Stern, G., Barber, D.G., 2017. An electromagnetic detection case study on crude oil injection in a young sea ice environment. IEEE Trans. Geosci. Remote Sens. 55 (8), 4465–4475.
Frankenstein, G., Garner, R., 1967. Equations for determining the brine volume of sea ice from -0.5 to -22.9°C. J. Glaciology 6 (48), 943–944.
Frantz, C.M., Light, B., Farley, S.M., Carpenter, S., Lieblappen, R., Courville, Z., Orellana, M.V., Junge, K., 2019. Physical and optical characteristics of heavily melted "rotten" Arctic Sea ice. Cryosphere 13, 775–793.
Fritsen, C.H., Lytle, V.I., Ackley, S.F., Sullivan, C.W., 1994. Autumn bloom of Antarctic pack-ice algae. Science 266, 782–784.
Fritt-Rasmussen, J., Wegeberg, S., Gustavson, K., 2015. Review on burn residues from in situ burning of oil spills in relation to Arctic waters. Water Air Soil Pollut. 226 (10), 329.
Fung, A.K., Liu, W.Y., Chen, K.S., Tsay, M.K., 2002. An improved iem model for bistatic scattering from rough surfaces. J. Electromagn. Waves Appl. 16, 689–702.
Galley, R.J., Else, B.G.T., Geilfus, N.-X., Hare, A.A., Isleifson, D., Barber, D.G., Rysgaard, S., 2015. Imaged brine inclusions in young sea ice - shape, distribution and formation timing. Cold Reg. Sci. Technol. https://doi.org/10.1016/j.coldregions.2014.12.011.
Golden, K.M., Eicken, H., Heaton, A.L., Miner, J., Pringle, D.J., Zhu, J., 2007. Thermal evolution of permeability and microstructure in sea ice. Geophys. Res. Lett. 34, L16501. https://doi.org/10.1029/2007GL030447.
Harsem, Ø., Eide, A., Heen, K., 2011. Factors influencing future oil and gas prospects in the Arctic. Energy Policy 39 (12), 8037–8045.
Hildebrand, T., Rüegsegger, P., 1997. Quantification of bone microarchitecture with the structure model index. Comput. Methods Biomech. Bio Med. Eng. 1 (1), 15–23.
Hubert, C., Stern, G., 2016-2017. GENICE: Microbial Genomics for Oil Spill Preparadness in Canada's Arctic Marine Environment. Genome Canada. www.genomecanada.ca/en/genice-microbial-genomics-oil-spill-preparedness-canadas-arctic-marine-environment.
Iassonov, P., Gebrenegus, T., Tuller, M., 2009. Segmentation of X-ray computed tomography images of porous materials: a crucial step for characterization and quantitative analysis of pore structures. Water Resour. Res. 45, W09415. https://doi.org/10.1029/2009WR008087.
IPCC, 2014. In: Team, Core Writing, Pachauri, R.K., Meyer, L.A. (Eds.), Climate Change 2014: Synthesis Report. Contribution of Working Groups I, II and III to the Fifth Assessment Report of the Intergovernmental Panel on Climate Change. IPCC, Geneva, Switzerland vols. 1 and 2.
Isleifson, D., Hwang, Byongjun, Barber, D.G., Scharien, R.K., Shafai, L., 2010. C-band polarimetric backscattering signatures of newly formed sea ice during fall freeze-up. IEEE Trans. Geosci. Remote Sens. 48, 3256–3267.
Isleifson, D., Galley, R.J., Barber, D.G., Landy, J.C., Komarov, A.S., Shafai, L., 2014. A study on the C-band polarimetric scattering and physical characteristics of frost flowers on experimental sea ice. IEEE Trans. Geosci. Remote Sens. 52 (3), 1787–1798.
Isleifson, D., Komarov, A., Desmond, D., Stern, G., Barber, D., 2020. Modeling backscattering from oil-contaminated sea ice using a multi-layered scattering method. In: Proceedings of the 2020 IEEE International Geoscience and Remote Sensing Symposium, pp. 1–2.
Ketcham, R., Carlson, W.D., 2001. Acquisition, optimization and interpretation of X-ray computed tomographic imagery: applications to the geosciences. Comput. Geosci. 27 (4), 381–400.
Krembs, C., Gradinger, R., Spindler, M., 2000. Implications of brine channel geometry and surface area for the interaction of sympagic organisms in Arctic Sea ice. J. Exp. Mar. Biol. Ecol. 243, 55–80.
Lieb-Lappen, R.M., Golden, E.J., Obbard, R.W., 2017. Metrics for interpreting the microstructure of sea ice using X-ray micro-computed tomography. Cold Reg. Sci. Technol. 138, 24–35. Web.
Lieblappen, R.M., Kumar, D.D., Pauls, S.D., Obbard, R.W., 2018. A network model for characterizing brine channels in sea ice. Cryosphere 12 (1013–1026), 2018. https://doi.org/10.5194/tc-12-1013-2018.
Li, T., Li, S., Zhao, J., Lu, P., Meng, L., 2012. Sphericitiesof non-spherical objects. Particuology 10, 97–104.
Martin, S., 1979. A field study of brine drainage and oil entrainment in first-Year Sea ice. J. Glaciol. 22 (88), 473–502.
Maus, S., Becker, J., Schneebeli, M., Wiegmann, A., 2015. Oil saturation of the sea ice pore space. In: Proceedings of the 23rd International Conference on Port and Ocean Engineering under Arctic Conditions. Web.
Maus, S., Leisinger, S., Matzl, M., Schneebeli, M., Wiegmann, A., 2013. Modelling oil entrapment in sea ice on the basis of 3d micro-tomographic images. In: Proceedings of the International Conference on Port and Ocean Engineering under Arctic Conditions.
Neusitzer, T.D., Firoozy, N., Tiede, T.M., Desmond, D.S., Lemes, M., Stern, G.A., Rysgaard, S., Mojabi, P., Barber, D.G., 2018a. Examining the impact of a crude oil spill on the permittivity profile and normalized radar cross-section of Young Sea ice. IEEE Trans. Geosci. Remote Sens. 56 (2), 921–936. https://doi.org/10.1109/tgrs.2017.2756843.
Neusitzer, T.D., Firoozy, N., Chirkova, D., Polcwiartek, K., Tiede, T., Desmond, D., Snyder, N., Lemes, M., Rysgaard, S., Wang, F., Smith, A., Hubert, C., Stern, G., Mojabi, P., Barber, D., 2018b. Remote sensing of oil spills in freezing environments at the university of manitoba sea-ice environmental research facility. In: Proceedings of the 18th International Symposium on Antenna Technology and Applied Electromagnetics (ANTEM), Waterloo, ON, CA, pp. 1–3.
Obbard, R., Troderman, G., Baker, I., 2009. J. Glaciol. 55, 1113–1115.
Oggier, M., Eicken, H., Wilkinson, J., Petrich, C., O'Sadnick, M., 2019. Crude oil migration in sea-ice: Laboratory studies of constraints on oil mobilization and seasonal evolution. Cold Reg. Sci. Technol. https://doi.org/10.1016/j.coldregions.2019.102924 accepted October 2019.
O'Sadnick, M.O., Petrich, C., Phuong, N.D., 2017. The entrainment and migration of crude oil in sea ice, the use of vegetable oil as a substitute, and other lessons from laboratory experiments. In: Proceedings of the 24th International Conference on Port and Ocean Engineering under Arctic Conditions, Busan, Korea.
Payne, J.R., Hachmeister, L.E., McNabb, G.D., Sharpe, H.E., Smith, G.S., Menen, C.A., 1991b. Brine-induced advection of dissolved aromatic hydrocarbons to Arctic bottom waters. Environ. Sci. Technol. 25, 940–951.
Payne, J.R., McNabb Jr., G.D., Clayton Jr., J.R., 1991a. Oil-weathering behavior in Arctic environments. Polar Res. 10 (2), 631–662.
Petrich, C., Eicken, H., 2010. Growth, structure and properties of sea ice. In: Sea Ice, Second edition. Wiley-Blackwell, United Kingdom (Ch 2).
Petrich, C., Karlsson, J., Eicken, H., 2013. Porosity of growing sea ice and potential for oil entrainment. Cold Reg. Sci. Technol. 87, 27–32. Web.
Polder, D., van Santen, J.H., 1946. The effective permeability of mixtures of solids. Physica 12 (5), 257–271.
Prince, R.C., Walters, C.C., 2016. Biodegradation of oil hydrocarbons and its implications for source identification. In: Standard Handbook Oil Spill Environmental Forensics: Fingerprinting and Source Identification, 2nd. Ch 19 accepted October 2019.
Pringle, D.J., Miner, J.E., Eicken, H., Golden, K.M., 2009. Pore space percolation in sea ice single crystals. J. Geophys. Res. 114, C12017. https://doi.org/10.1029/2008JC005145.
Puestow, T., Parsons, L., Zakharov, I., Cater, N., Bobby, P., Fuglem, M., Parr, G., Jayasiri, A., Warren, S., Warbanski, G., 2013. Oil spill detection and mapping in low visibility and ice: surface remote sensing. In: Arctic Response Technology Oil Spill Preparedness, Final Report 5.1.
Salomon, M.L., Arntsen, M., Phuong, N.D., Maus, S., O'Sadnick, M., Petrich, C., Schneebeli, M., Wiese, M., 2017. Experimental and micro-CT study on the oil distribution in laboratory grown sea ice. In: Proceedings of the 24th International Conference on Port and Ocean Engineering under Arctic Conditions. Busan, Korea.
Saltymakova, Smith, A.F., Polcwiartek, K., Desmond, D., Snyder, N., Wolfe, T., Bautista, M.A., Stone, M., Ellefson, E., Hubert, C., Stern, G.A., 2019. Enriched Arctic bacteria potential for biodegradation of polycyclic aromatic hydrocarbons estimated from crude oil-in-ice mesocosm experiment. In: Proceedings of the 42nd AMOP Technical Seminar on Environmental Contamination and Response. https://www.researchgate.net/publication/334151994.
Saltymakova, D., Desmond, D.S., Isleifson, D., Firoozy, N., Neusitzer, T.D., Xu, Z., Lemes, M., Barber, D.G., Stern, G.A., 2020. Effect of dissolution, evaporation, and photooxidation on crude oil chemical composition, dielectric properties and its radar signature in the Arctic environment. Mar. Pollut. Bull. 151, 110629.

Schenk, 2011 C.J. Schenk 2011 Chapter 41 Geology and petroleum potential of the West Greenland-East Canada Province Geol. Soc. Lond. Mem. 351 627645 Web.
Sezgin, M., Sankur, B., 2004. Survey over image thresholding techniques and quantitative performance evaluation. J. Electron. Imaging 13, 146–165. https://doi.org/10.1117/1.1631315.
Smith, L.C., Stephenson, S.R., 2013. New Trans-Arctic shipping routes navigable by midcentury. Proc. Natl. Acad. Sci. 110 (13) n. pag. Web.
Tinga, W.R., Voss, W.A.G., Blossey, D.F., 1973. Generalized approach to multiphase dielectric mixture theory. J. Appl. Phys. 44 (9), 3897–3902.
Ulaby, F.T., Long, D.G., 2014. University of Michigan Press, Ann Arbor, MI.
Vancoppenolle, M., Meiners, K.M., Michel, C., Bopp, L., Brabant, F., Carnat, G., Delille, B., Lannuzel, D., Madec, G., Moreau, S., Tison, J.-L., van der Merwe, P., 2013. Role of sea ice in global biogeochemical cycles: emerging views and challenges. Quaternary Sci. Rev. 79, 207–230. https://doi.org/10.1016/j.quascirev.2013.04.011.
L. Vergeynst K.U. Kjeldsen P. Lassen S. Rysgaard 2018 Bacterial Community Succession and Degradation Patterns of Hydrocarbons in Seawater at Low Temperature.
Wadell, H., 1935. Volume, shape, and roundness of quartz particles. J. Geol. 43 (3), 250–280.
W. F. Weeks S. F. Ackley The growth, structure and properties of sea ice The Geophysics of Sea Ice N. Untersteiner Plenum Press New York 9164 1986.
Wilkinson, J.P., Boyd, T., Hagen, B., Maksym, T., Pegau, S., Roman, C., Singh, H., Zabilansky, L., 2015. Detection and quantification of oil under sea ice: the view from below. Cold Reg. Sci. Technol. 109, 9–17.